All-optical spatial light modulator for reconfigurable silicon photonic circuits

Roman Bruck,[1] Kevin Vynck,[2] Philippe Lalanne,[2] Ben Mills,[3] David J. Thomson,[3] Goran Z. Mashanovich,[3] Graham T. Reed,[3] and Otto L. Muskens[1,*]

[1] *Physics and Astronomy, Faculty of Physical Sciences and Engineering, University of Southampton, Southampton SO17 1BJ, UK*
[2] *LP2N, UMR 5298, CNRS–IOGS–University of Bordeaux, 33400 Talence, France*
[3] *Optoelectronics Research Centre, University of Southampton, Southampton SO17 1BJ, UK*
**Corresponding author: o.muskens@soton.ac.uk*

Received 13 January 2016; revised 11 March 2016; accepted 11 March 2016 (Doc. ID 257373); published 5 April 2016

Reconfigurable photonic devices capable of routing the flow of light enable flexible integrated-optic circuits that are not hardwired but can be externally controlled. Analogous to free-space spatial light modulators, we demonstrate all-optical wavefront shaping in integrated silicon-on-insulator photonic devices by modifying the spatial refractive index profile of the device employing ultraviolet pulsed laser excitation. Applying appropriate excitation patterns grants us full control over the optical transfer function of telecommunication-wavelength light traveling through the device, thus allowing us to redefine its functionalities. As a proof of concept, we experimentally demonstrate the routing of light between the ports of a multimode interference power splitter with more than 97% total efficiency and negligible losses. Wavefront shaping in integrated photonic circuits provides a conceptually new approach toward achieving highly adaptable and field-programmable photonic circuits with applications in optical testing and data communication.

OCIS codes: (130.3120) Integrated optics devices; (230.1150) All-optical devices; (130.0130) Integrated optics; (190.4390) Nonlinear optics, integrated optics; (230.7400) Waveguides, slab; (230.6120) Spatial light modulators.

http://dx.doi.org/10.1364/OPTICA.3.000396

1. INTRODUCTION

With optical links replacing electrical connections on ever shorter length scales, all-optical control of optical signals becomes ever more desirable to circumvent the electronic speed limit and avoid transformation losses between optical and electrical domains. All-optical switches and modulators have been demonstrated based on different integrated optical designs [1–9]. Most of the conventional tuneable photonic devices use one specific parameter to establish precise control over the output(s), but lack the freedom to completely govern the transmission function. For static devices, many new degrees of freedom can be accessed by exploiting the vast design space offered by complex device geometries [10–14]. In fact, defining the spatial refractive index profile in a small planar area is sufficient to create compact devices with arbitrary characteristics, as was recently demonstrated experimentally by etching an optimized pattern into a silicon-on-insulator (SOI) slab [15].

Here we show that spatial refractive index profiles can be controlled all-optically, allowing us to dynamically route light between outputs of a SOI multimode interference (MMI) device. Our approach uses the vast capabilities offered by digital micromirror device (DMD) technology in spatial light modulation in conjunction with an ultrafast photomodulation setup [16]. As shown in Fig. 1(a), a DMD is used to project a pattern of femtosecond laser pulses onto the MMI device surface, allowing simultaneous modulation of the refractive index in a large number (around 500) of positions. For each illuminated position, plasma dispersion locally decreases the refractive index of silicon by approximately 0.25 refractive index units (see Supplement 1), thus achieving a significant perturbation of the light flow in the device. Wavefront shaping has been demonstrated as a powerful tool in both characterizing and controlling the optical modes in three-dimensional complex media [17–19]. Translating these capabilities to an integrated platform opens up significant opportunities for freeform shaping of optical signals in integrated photonic circuits. We specifically demonstrate this general technique on the example of shaping wavefronts in SOI MMI regions effectively and with negligible loss. The transfer function of MMI devices is defined by the interference of a large number of transverse modes. Any localized perturbation in the refractive index profile introduces coupling and a redistribution of power between MMI modes [see Figs. 1(b) and 1(c)]. Considering a single perturbation, modeled by a refractive index change $\Delta n = -0.25$ over a square 700 nm × 700 nm pixel, we find with rigorous coupled-mode simulations [20] that up to 10% of the power carried by one incident mode can be redistributed to other forward-propagating modes [see Fig. 1(c)]. Backscattering with at most 0.1% is negligible. The general trend is that coupling is most efficient between adjacent modes (near the diagonal).

2334-2536/16/040396-07 Journal © 2016 Optical Society of America

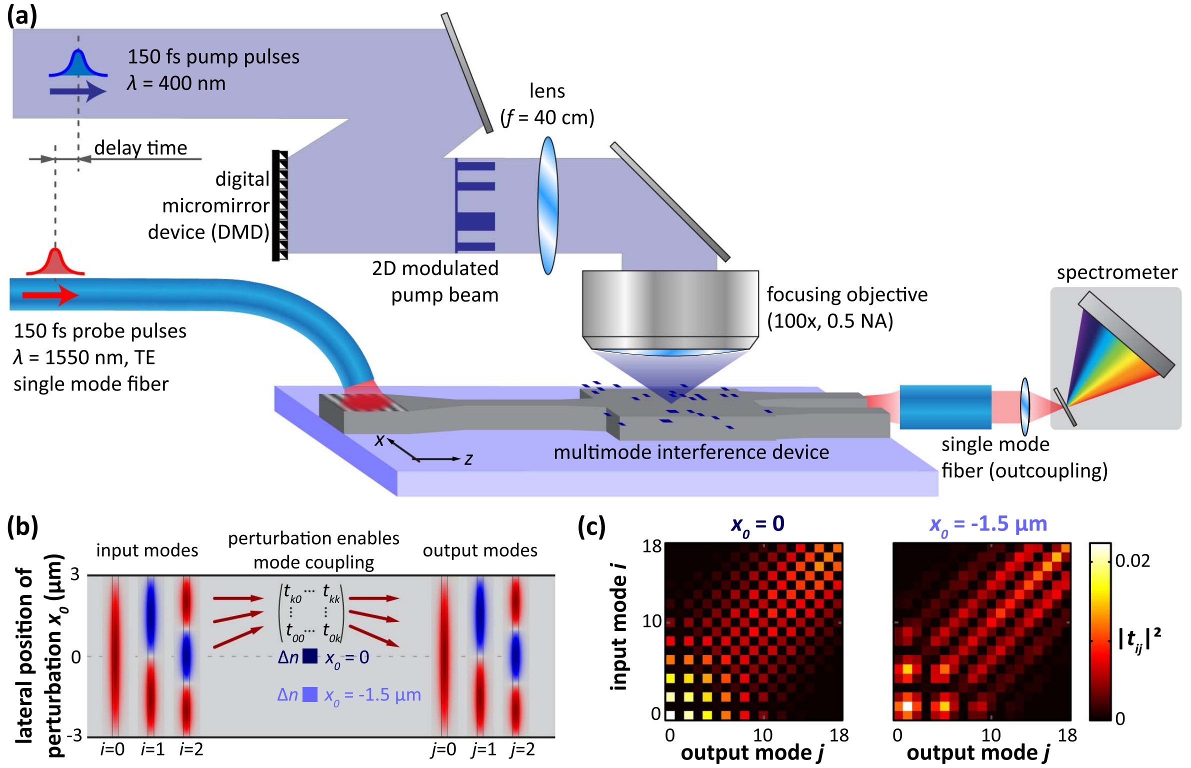

Fig. 1. Concept of wavefront shaping by ultrafast photomodulation spectroscopy. (a) In the experiments, transmission spectra of TE-polarized 150 fs probe pulses with a central wavelength of 1550 nm are monitored through a multimode interference (MMI) device. Simultaneously, a 2D pattern of 400 nm pump light is projected onto the device (blue overlay), locally decreasing the refractive index of the silicon MMI material by plasma dispersion. The pump beam is spatially modulated by employing a digital micromirror device (DMD), and the pattern of the DMD is imaged onto the MMI surface by means of a lens and a microscope objective. (b) Each point of the pump pattern induces a perturbation in the refractive index profile of the MMI, enabling coupling between MMI modes, thus allowing shaping of the mode interference pattern at the MMI output plane. (c) Visual representation of the power mode coupling matrix for refractive index perturbations ($\Delta n = -0.25$, size 700 nm × 700 nm) at two lateral positions. Calculated from a-FMM simulations, these values correspond to the fraction of power that is exchanged between modes due to the perturbation.

As the coupling efficiency depends on the mode amplitudes at the lateral position x_0 of the perturbation, choosing x_0 allows us to define how power is redistributed. For instance, perturbations at the MMI center couple only modes exhibiting the same symmetry, while off-center perturbations allow coupling between all modes. Additionally, every individual perturbation introduces a weak phase shift (≈0.1 rad). Thus, a perturbation pattern, composed of tens of local perturbations, gives control over the distribution of power into the transverse modes as well as their phase relations, and may eventually change the intensity pattern at the output plane/port to any desired form. By addressing all degrees of freedom of the MMI device, that is, the mode power distribution and the mode phase relations, our technique grants total control over the transfer function of the device.

MMI devices with tunable power-splitting ratios have been analyzed using the particular properties of self-images formed at intermediate distances inside the MMI [21–23]. Tuning of the refractive index using thermal or electro-optic elements positioned at these specific intermediate cross-sectional planes allows control of the asymmetry of the self-images at the output using a single control parameter. While such multimode interference power splitters (MIPSs) are of technological interest, they provide only a limited range of tuning capabilities while requiring relatively large device footprints of several hundreds of micrometers in length [21–25]. Compared to the output-balancing characteristics of MIPS designs, wavefront shaping relies on a distributed phase control over the entire volume of the MMI device and offers *full* control over the transfer matrix in devices that are at least an order of magnitude less in length. The MMI device (220 nm thick silicon slab of size 6 µm × 31.87 µm) under investigation is a standard component in state-of-the-art silicon photonics and was experimentally verified to have insertion losses below 1 dB [26].

2. THEORETICAL ANALYSIS OF THE WAVEFRONT SHAPING MECHANISM

To understand how a small set of local perturbations can redirect the propagating light toward any specific output port and to evaluate the approach for all-optical routing purposes, we resort to 2D coupled-mode simulations, performed with a fully vectorial aperiodic Fourier modal method (a-FMM) [20] (see Methods section in Supplement 1; $\lambda = 1550$ nm, TE polarization). This method calculates the modes in a Fourier basis, using a supercell method and perfectly matched layers. It relies on a scattering matrix formalism to accurately describe the coupling between modes propagating in the input waveguide, MMI, and output waveguides. Figure 2(a) (left) shows the electric field map of the unperturbed MMI. Without fit parameters, simulations confirm the optimized MMI design with transmission exceeding

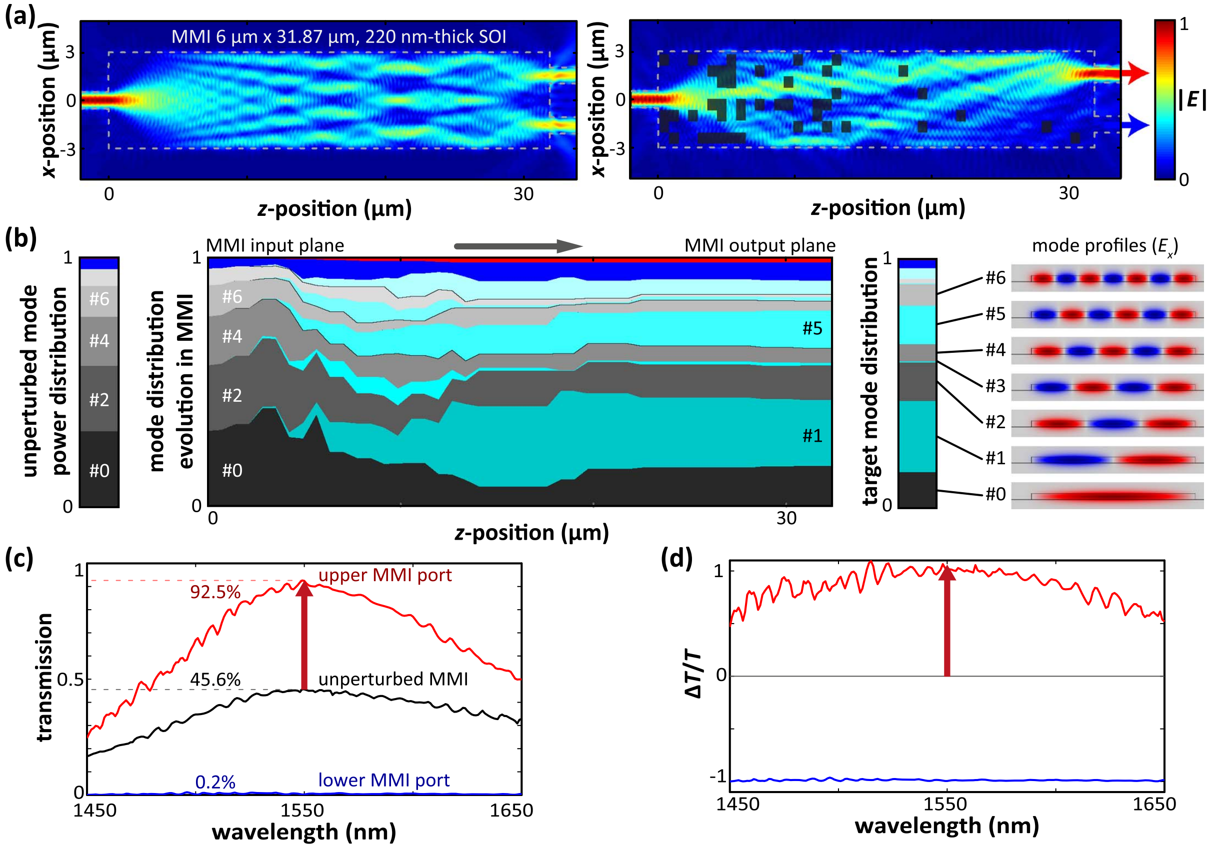

Fig. 2. Numerical coupled-mode simulations. (a) Electric field maps of the unperturbed MMI (left) and the MMI with a perturbation pattern with $\Delta n = -0.25$ (right), as indicated by the black overlay, from a-FMM simulations. The perturbation pattern was numerically optimized for maximum transmission into the upper MMI output port. (b) The injected light from the centrally placed input waveguide excites only even (symmetric) MMI modes at the input plane of the MMI (left graph). Due to the perturbation pattern, power is transferred from even modes (gray shades) into odd (antisymmetric) modes (cyan shades) as the light propagates through the MMI (center graph). The 10 lowest-order modes are plotted explicitly. For clarity, we combine the remaining nine MMI modes as they carry only a little energy (blue area). Losses due to the perturbation pattern are shown in red. The resulting mode distribution interferes at the output plane of the MMI and steers the light effectively toward the upper output. We compare this mode distribution with the numerically ideal mode distribution (right graph) for maximum overlap with the output waveguide mode. The insets depict cross-sectional electric field profiles of the MMI modes calculated with Comsol Multiphysics. (c), (d) Spectral behavior of the beam steering effect produced by the optimized perturbation pattern. Transmissions into the fundamental modes of the top (T_{top}, red curve) and bottom (T_{bot}, blue curve) output waveguides remain >85% and <1% for a 60 nm bandwidth, respectively. The spectrum of the unperturbed MMI (T_{ref}) is shown as a black curve. The resulting transmission enhancement, $\Delta T/T = (T_{\mathrm{top}} - T_{\mathrm{ref}})/T_{\mathrm{ref}}$, and suppression, $\Delta T/T = (T_{\mathrm{bot}} - T_{\mathrm{ref}})/T_{\mathrm{ref}}$, are similarly broadband.

91% (<0.5 dB loss) to the fundamental modes of the output waveguides (45.6% each).

The on-axis input waveguide excites even (i.e., symmetric) MMI modes only, as shown in the left graph of Fig. 2(b). In an unperturbed MMI, modes would not exchange power and the mode power distribution would remain constant as light propagates through the MMI, resulting in a symmetric output profile. However, the inclusion of perturbations yields a redistribution of the incident power between MMI modes. The possibility of imprinting the desired modal phase and power distributions is the key to forming a targeted intensity profile at the MMI output facet. For instance, maximizing light transmission to a single off-axis output port requires significant feeding of power to certain odd (i.e., antisymmetric) modes. About 50% of the total power is required in odd modes, mostly in modes #1, #5, and #9. The right graph in Fig. 2(b) gives the target mode distribution needed for perfect overlap with the waveguide mode of the upper port. As the output waveguides feature 1 µm wide tapers, and thus a comparatively wide intensity profile, high-order MMI modes with high spatial frequencies (#10 to #18) contribute only weakly to the interference pattern. Narrower waveguides would require stronger contributions from high-order modes.

While single perturbations lack sufficient strength to excite asymmetric modes strongly, we show that a set of perturbations can be designed to collectively reach the desired requirement. To numerically optimize the perturbation pattern, we divide the MMI area into 700 nm wide square pixels and use a random walk process to create a Markov chain in the pixel state space. Considering that backreflection is negligible, the random walk sequence should follow the direction of the light flow (z direction). Starting from the unperturbed MMI, the pixels are visited columnwise from the input plane toward the output plane. Within each column (x direction), pixels are addressed in a random sequence, each pixel being addressed exactly once. For each visit, we calculate the transmission into the fundamental mode of the output waveguides with the a-FMM for the perturbed ($\Delta n = -0.25$) pixel and add it to the set only if the transmission to the desired output port increases. The perturbation pattern is thus progressively constructed with each optimization step, while the MMI performance is adjusted toward its desired characteristic. Due to its stochastic nature, each optimization process yields a different perturbation pattern, yet we have observed that variations in the final performance are only marginal (1%–2% standard deviation on the optimized transmission). Figure 2(a) (right) shows the electric field map of the MMI for an optimized perturbation pattern, while the center graph in Fig. 2(b) concurrently visualizes the evolution of the MMI mode power distribution as light propagates through this perturbed MMI. The generated mode power distribution at the output plane of the MMI almost perfectly matches the ideal distribution (right graph). Losses (red) due to scattering into radiation modes and backreflection are below 2%.

The calculated transmission spectra of the MMI with the optimized perturbation pattern are shown in Fig. 2(c). The transmission of the unperturbed MMI (black) is increased in the upper port, with the transmission into the fundamental mode of the upper port reaching ~92.5% (−0.3 dB), surpassing the transmission of the unperturbed device (~91% in both ports) due to enhanced mode matching at the output plane. Additionally, cross talk is very weak, with a transmission of only 0.2% (−27 dB) in the guided mode of the lower port. When expressed in terms of relative transmission changes ($\Delta T/T$), which may be measured experimentally more accurately than absolute transmission, $\Delta T/T$ reaches and exceeds values of 1 for the upper port and is getting close to −1 for the lower port [see Fig. 2(d)]. It is interesting to note that the beam steering effect of a single perturbation pattern is effective on a broad wavelength range. The high transmission and very low cross talk on a broad spectral range mark the excellent performance of the device. In Fig. (S1) of Supplement 1, we further show that the excellent performance resists various experimental errors or uncertainties in the exact pattern position and perturbation strength.

3. EXPERIMENTAL REALIZATION OF ALL-OPTICAL ROUTING

The optical system used for the all-optical routing of light comprises a Ti:sapphire laser coupled with an optical parametric amplifier, providing 150 fs pulses at 1550 nm and a second harmonic output at 400 nm. The 400 nm pump beam is spatially modulated by the DMD, and the pattern of the DMD is imaged onto the MMI surface [see setup in Fig. 1(a)]. A detailed description is presented in Supplement 1. Experiments were done using a pump pixel width on the sample of 700 nm and a fluence of 64 pJ/μm, resulting in a pump-induced change in the real part of the refractive index of around −0.25.

The experimental demonstration follows a similar scheme to the numerical calculations to optimize the digital pixel pattern of the DMD. For this purpose, we divided the MMI area into nine regions of 10 vertical by 5 horizontal pixels and optimized each region in ascending order by performing 100 optimization steps (on average, two visits per pixel are performed to reduce influence from laser noise). Figure 3(a) illustrates the experimental optimization process to maximize $\Delta T/T$ of the upper output of the

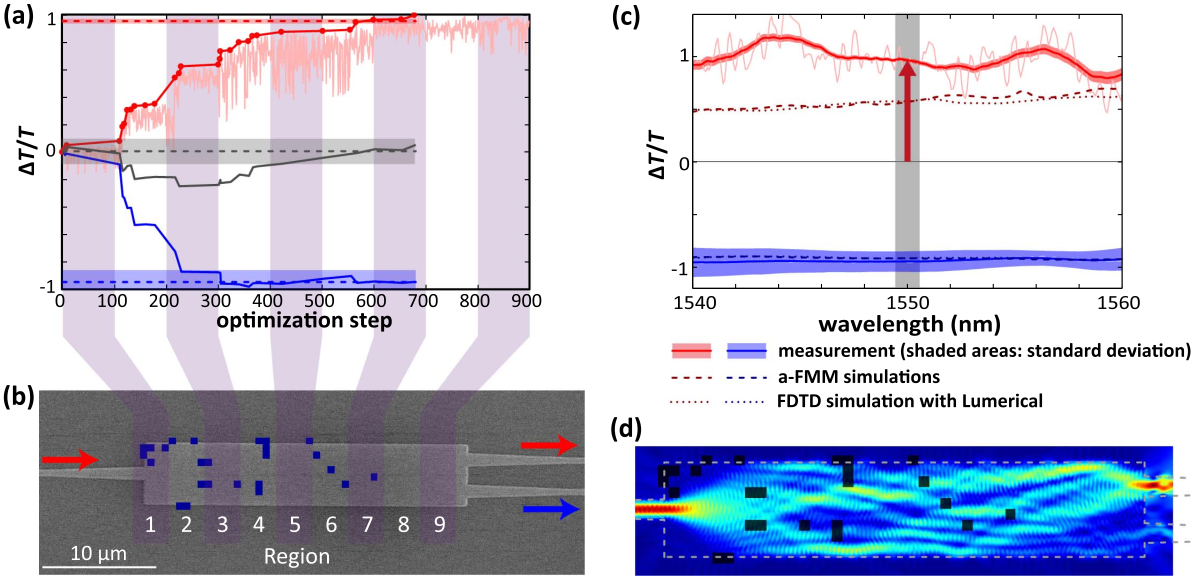

Fig. 3. Digital micromirror device pattern optimization. (a) Experimental optimization run to maximize transmission in a wavelength window of 1550 ± 1.7 nm through the upper output port of the MMI. The individual regions (numbered from 1 to 9, 10 × 5 pixels each) are optimized individually in ascending order by performing 100 optimization steps in each region. In each step, a random pixel in the region under optimization is flipped, changing the transmission through the upper output port. The thin red line gives the change in transmission $\Delta T/T$ between the perturbed and unperturbed state for each step. Only pixels resulting in an increased $\Delta T/T$ are accepted (dots with thick red line), and the new DMD configuration is stored. In a subsequent measurement, all stored DMD configurations are reapplied while monitoring the lower MMI output (thick blue line). The excess losses induced in the MMI are calculated as the sum of $\Delta T/T$ of both outputs (thick gray line). After finishing the optimization run, we averaged 50 measurements with the final DMD configuration to determine the optimized $\Delta T/T$ for both ports minimally influenced by laser noise (horizontal dashed lines; shaded areas give the standard deviation). (b) SEM picture of the MMI device overlaid with the final DMD configuration (blue) and indications of the regions used for the optimization. (c) $\Delta T/T$ spectra with the final DMD configuration for the two MMI outputs (thick solid lines; upper output red, lower output blue, shaded areas give the standard deviation), compared with simulated $\Delta T/T$ spectra from a-FMM (dashed lines) and the FDTD method (dotted lines). The red arrow and the gray shaded area indicate the wavelength window used for optimization. (d) Simulated electric field maps from a-FMM ($\lambda = 1550$ nm) for the MMI, where for each pixel of the experimentally optimized pattern (black overlay) the effective index is reduced by 0.25.

MMI device in a wavelength window of 1550 ± 1.7 nm. The thin red curve gives the evolution of $\Delta T/T$ of the upper port at each optimization step. Every time a new transmission maximum is achieved, the DMD configuration is accepted (dots on the thick red line). After completing the optimization of the upper port, we analyze the transmission of the lower port in a subsequent experiment by reapplying all stored DMD configurations while measuring the lower-port transmission (thick blue line). We then calculate the induced excess losses (gray line) by our modulation technique as the sum of $\Delta T/T$ of both outputs. To minimize the influence of laser noise on our results, we averaged 50 measurements with the final DMD configuration for both outputs (horizontal dashed lines with shaded areas giving the standard deviation). The optimization shown in Fig. 3(a) was performed at a delay time between the pump and probe pulses of 10 ps, meaning that pump pulses arrive at the MMI 10 ps before the probe pulses. For the final DMD configuration consisting of 25 active pixels, the transmission into the upper MMI output could be increased by more than 95% ($\Delta T/T = 0.96 \pm 0.02$), efficiently routing almost all (>97.5%) transmitted light into one output. From $\Delta T/T = -0.95 \pm 0.09$ for the lower output, we deduct that excess losses are smaller than the accuracy of our experimental setup. Figure 3(b) shows a scanning electron microscope (SEM) micrograph of the MMI device overlaid (blue) with the pump light pattern that evolved in the optimization process. As in the simulations, we observe that the pixels are distributed over the MMI in a highly irregular pattern, showing the fundamental difference with MIPSs based on intermediate self-imaging conditions [21–25].

Figure 3(c) shows the final $\Delta T/T$ spectra after optimization (solid lines) and compares these with the numerical results from the a-FMM (dashed lines) and finite-difference time-domain (FDTD) method (dotted lines) using the experimental perturbation pattern ($\Delta n = -0.25$).

The resulting a-FMM electric field map in Fig. 3(d) confirms the beam steering effect, resulting in a field profile at the MMI output plane that matches the selected output waveguide. The difference in magnitude of the output enhancement between experimental and numerical spectra in Fig. 3(c) is due to the fact that simulations do not reflect experimental imperfections, such as inhomogeneity of the pump intensity over the DMD area, diffraction effects, and aberrations, which lead to deviations from the ideal pixel shape at the sample surface.

Nevertheless, it is important to note that the experimental optimization procedure naturally takes into account and “corrects” all these imperfections, resulting in enhancement levels comparable to those of the numerically optimized MMI shown in Fig. 2. A strong enhancement of the transmission is achieved experimentally over the entire observed 20 nm wavelength range, demonstrating the broadband characteristics of the integrated spatial light modulator. Similar to the numerical results, $\Delta T/T$ values larger than 1 are possible, as the optimization can result in an increase in the overall device transmission compared to the unperturbed state. Averaged over the whole 20 nm wide wavelength window, we find an average $\Delta T/T$ in the upper waveguide of 0.98 ± 0.1, and −0.94 ± 0.09 in the lower waveguide. The sensitivity of the pump pattern alignment was investigated both theoretically and experimentally in Figs. (S1) and

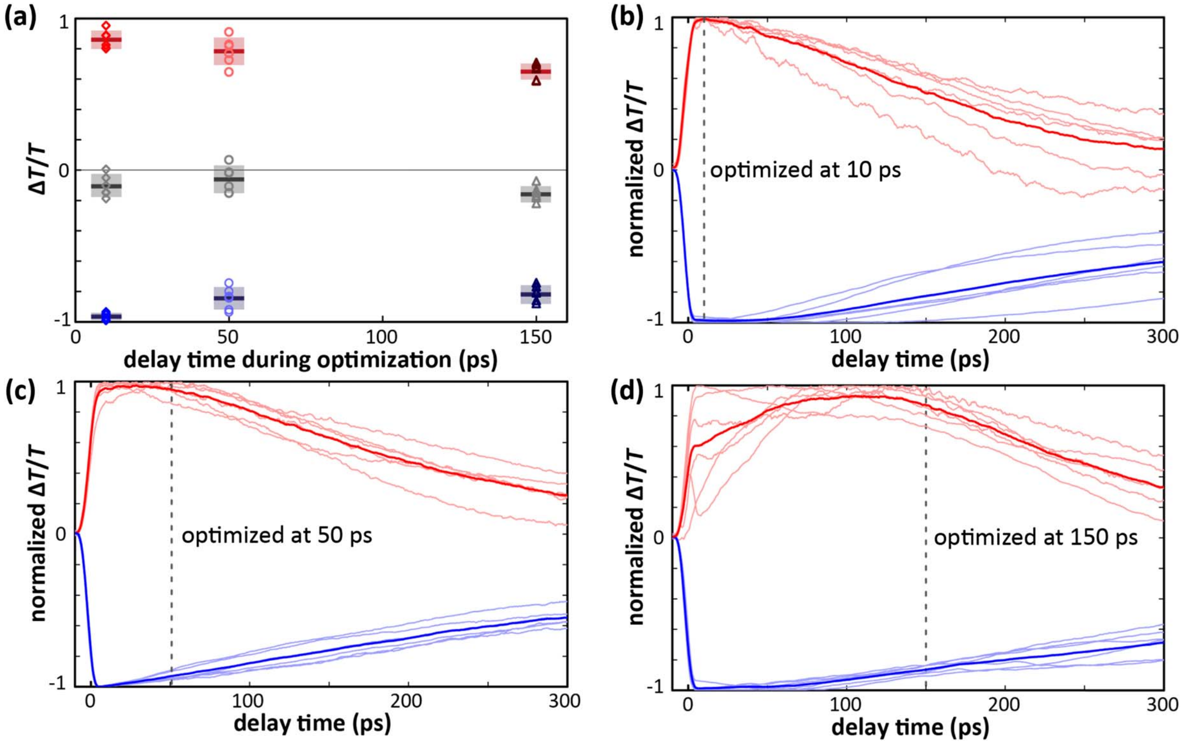

Fig. 4. Time characteristics of excitation. (a) $\Delta T/T$ values with DMD configurations after optimizations were performed for three different delay times (diamonds, 10 ps; circles, 50 ps; triangles, 150 ps; six values each). Thick horizontal lines give the group average, and the shaded areas indicate the standard deviation. (b)–(d) Time characteristics induced by different pump light patterns (thin lines) optimized at different delay times: (b) 10 ps, (c) 50 ps, (d) 150 ps. These curves are normalized to their individual $\Delta T/T$ maximum. Further, the averages (thick lines) of the six-curve groups are given. We note that the averages are based on normalized curves, but are not normalized themselves. Thus, they do not necessarily reach a value of 1 or −1.

(S2) of Supplement 1. It is found that perturbation patterns have alignment tolerances of less than 1 μm in both the propagation and transverse directions. This sensitivity reveals the delicate coupling between many degrees of freedom in a complex system, with an output pattern that is the result of many subsequent perturbations acting in concert.

The spatial optimization is the result of a series of local perturbations that depend on time as the system evolves from excited states induced by the ultrafast pump pulses. To investigate the role of time dynamics, perturbation patterns were optimized for different delay times (10, 50, and 150 ps), with the results summarized in Fig. 4(a). For longer delay times, the probe light experiences smaller refractive index perturbations as the free carriers excited by the pump are given more time to recombine [see Fig. (S3) in Supplement 1]. As a result, the largest increase in transmission could be obtained for the shortest delay time of 10 ps, where the average $\Delta T/T = 0.86 \pm 0.06$, with the average residual light transmission in the other output under 4%. At longer delay times, maximum enhancements are reduced. However, even at 150 ps, which is of the order of the free-carrier lifetime of 174 ps, transmission increases exceeding 65% can be achieved. The time characteristics of the optimized devices are analyzed in Figs. 4(b)–4(d). As expected, the maximum effect is mostly achieved around the delay time at which the optimization was performed. Furthermore, configurations optimized at 10 ps show the fastest decay, with a recovery time of around 190 ps. Optimizations at longer delay times result in slower initial rise and recovery times of the device, with a 100 ps long plateau of nearly constant performance.

Different optimization runs generally resulted in individual patterns because of the randomness introduced in the iterative process, and due to intrinsic noise present in the experimental system. However, general trends could be observed in the relative contributions of different parts of the MMI. In Fig. 5(a), the average $\Delta T/T$ obtained per region is revealed for the set of 18 experiments of Fig. 4, while Fig. 5(b) gives the average number of pixels accepted. Clearly, regions 2 to 4 are the most active and contribute strongly to the optimization process, with the greatest increase in transmission and the most pixels accepted. On average, 43.8 pixels are accepted per run, representing less than 10% of the MMI area and showing that a relatively small number of perturbations is sufficient to efficiently shape wavefronts in silicon devices. In the 2D map displayed in Fig. 5(c), the acceptance probability for each pixel position is given for an optimization of the upper output.

Wavefront shaping in silicon photonics holds potential for a wide range of device applications. We foresee many ways for further optimization of this concept, for example using the additional degrees of freedom in high-resolution DMD spatial light modulators to develop gradient designs based on transformation optics, or the use of phase change layers for writing nonvolatile patterns for reconfigurable optical memory devices. Once optimized patterns have been obtained using the relatively slow iterative process, they can be stored in a library, or imprinted using other techniques such as amplitude masks or multiple beam steering and applied at high frequencies. Ultimately, the switching speed is limited by the recombination of the free carriers in the silicon region, which was measured below 200 ps. Several schemes can be employed to further reduce the carrier lifetimes. Passive approaches include increasing the number of recombination sites by doping or ion implantation [27] or the modification of the silicon surface [28]. Further, free carriers can be depleted actively by contacting the silicon region with electrodes and operating the device under a reverse DC bias [29]. In addition to optimizing spatial degrees of freedom in broadband devices, it will be possible to design optical systems with wavelength dependent responses and to use wavefront shaping to achieve spectral control, or specific time domain characteristics, similar to their three-dimensional counterparts.

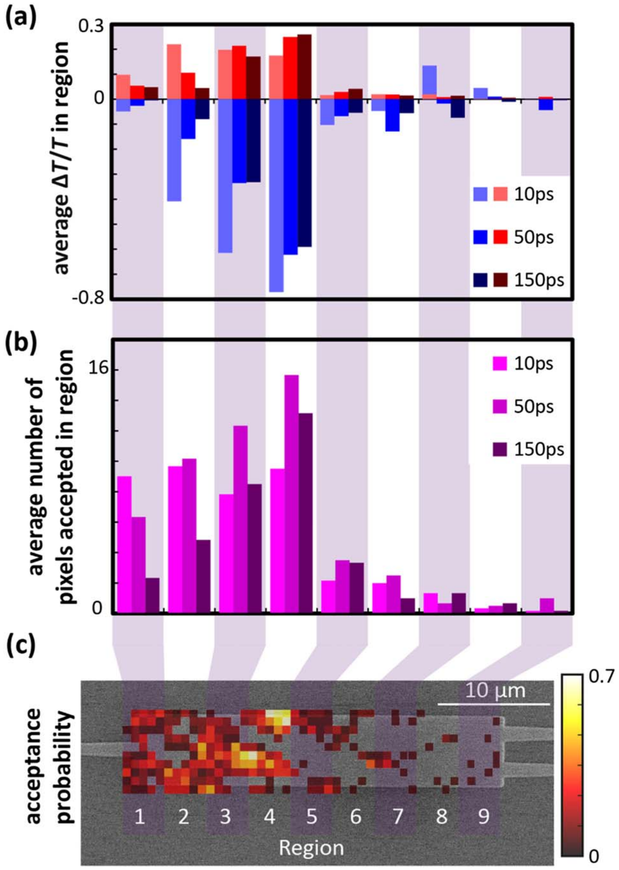

Fig. 5. Contribution of individual MMI regions. (a) Average $\Delta T/T$ per region in the experiments presented in Fig. 4. The total $\Delta T/T$ achieved during the optimization is the sum of $\Delta T/T$ values in the individual regions. (b) Average numbers of pixels accepted per region during the optimization processes. (c) Map of the probability that individual pixels are accepted during optimization.

4. CONCLUSIONS

In summary, we showed that arbitrary high-contrast ($\Delta n = -0.25$) binary refractive index profiles can be generated in planar silicon exploiting plasma dispersion from all-optical excitation with spatially modulated pump beams. We experimentally realized dynamic routing of light in a 1 × 2 MMI power splitter to any output port with better than 97% efficiency, cross talk below −27 dB, and negligible losses. Ultimately limited by the free-carrier recombination time in the MMI, switching speeds in the gigahertz regime could potentially be reached.

Our theoretical considerations indicate that by addressing the mode power distribution and the mode phase relations, our technique can exercise full control over the device transmission function and generate arbitrary intensity patterns at the output facet of the device.

Thus, we turn one of the most common passive optical elements into a versatile platform for reconfigurable silicon photonics.

We believe that this integrated distributed control is a new and effective approach for parallel dynamic control of degrees of freedom, and that the concept presented can be easily extended for more complex devices, for instance, with several output ports. In addition, this distributed approach can be viewed as the integrated-optics analog of volume holograms and thus may benefit from the additional degrees of freedom of volume holography [30]. This new concept of integrated spatial light modulation in silicon thus opens up avenues to all-optical reconfigurable devices, with possible applications in the testing of optical circuits and reconfigurable multiport optical filters, splitters, and modulators for data communication. By enlarging the area in which the refractive index profile can be defined, arbitrary light paths could, in principle, be realized all-optically, which would provide a similar level of flexibility to the electronic field-programmable gate array (FPGA). FPGA-like optical structures have been discussed, e.g., for microwave [31] and silicon nitride waveguides [32]. An all-optical FPGA analog based on the mature silicon photonics platform could be employed for a large number of applications in optical communications, e.g., in multiplexing, wavelength-selective switching, and routing.

Dataset citation. The dataset for this paper can be found at [33].

Funding. Engineering and Physical Sciences Research Council (EPSRC) (EP/J016918); Royal Society.

Acknowledgment. Goran Z. Mashanovich acknowledges support from the Royal Society through a University Research Fellowship.

See Supplement 1 for supporting content.

REFERENCES

1. V. R. Almeida, C. A. Barrios, R. R. Panepucci, and M. Lipson, “All-optical control of light on a silicon chip,” Nature **431**, 1081–1084 (2004).
2. C. Koos, P. Vorreau, T. Vallaitis, P. Dumon, W. Bogaerts, R. Baets, B. Esembeson, I. Biaggio, T. Michinobu, F. Diederich, W. Freude, and J. Leuthold, “All-optical high-speed signal processing with silicon-organic hybrid slot waveguides,” Nat. Photonics **3**, 216–219 (2009).
3. L. Liu, R. Kumar, K. Huybrechts, T. Spuesens, G. Roelkens, E.-J. Geluk, T. de Vries, P. Regreny, D. Van Thourhout, R. Baets, and G. Morthier, “An ultra-small, low-power, all-optical flip-flop memory on a silicon chip,” Nat. Photonics **4**, 182–187 (2010).
4. A. Martinez, J. Blasco, P. Sanchis, J. V. Galán, J. García-Rupérez, E. Jordana, P. Gautier, Y. Lebour, S. Hernández, R. Spano, R. Guider, N. Daldosso, B. Garrido, J. M. Fedeli, L. Pavesi, and J. Martí, “Ultrafast all-optical switching in a silicon-nanocrystal-based silicon slot waveguide at telecom wavelengths,” Nano Lett. **10**, 1506–1511 (2010).
5. K. Nozaki, T. Tanabe, A. Shinya, S. Matsuo, T. Sato, H. Taniyama, and M. Notomi, “Sub-femtojoule all-optical switching using a photonic-crystal nanocavity,” Nat. Photonics **4**, 477–483 (2010).
6. T. Tanabe, M. Notomi, S. Mitsugi, A. Shinya, and E. Kuramochi, “All-optical switches on a silicon chip realized using photonic crystal nanocavities,” Appl. Phys. Lett. **87**, 151112 (2005).
7. Y. Vlasov, W. M. Green, and F. Xia, “High-throughput silicon nanophotonic wavelength-insensitive switch for on-chip optical networks,” Nat. Photonics **2**, 242–246 (2008).
8. Y. H. Wen, O. Kuzucu, M. Fridman, A. L. Gaeta, L.-W. Luo, and M. Lipson, “All-optical control of an individual resonance in a silicon microresonator,” Phys. Rev. Lett. **108**, 223907 (2012).
9. R. Bruck, B. Mills, D. J. Thomson, B. Troia, V. M. N. Passaro, G. Z. Mashanovich, G. T. Reed, and O. L. Muskens, “Picosecond optically reconfigurable filters exploiting full free spectral range tuning of single ring and Vernier effect resonators,” Opt. Express **23**, 12468–12477 (2015).
10. V. Liu, Y. J. Liao, D. A. B. Miller, and S. Fan, “Design methodology for compact photonic-crystal-based wavelength division multiplexers,” Opt. Lett. **36**, 591–593 (2011).
11. V. Liu, D. A. B. Miller, and S. Fan, “Ultra-compact photonic crystal waveguide spatial mode converter and its connection to the optical diode effect,” Opt. Express **20**, 28388–28397 (2012).
12. J. S. Jensen and O. Sigmund, “Topology optimization for nanophotonics,” Laser Photon. Rev. **5**, 308–321 (2011).
13. Q. Wu, J. P. Turpin, and D. H. Werner, “Integrated photonic systems based on transformation optics enabled gradient index devices,” Light Sci. Appl. **1**, e38 (2012).
14. D. Liu, L. H. Gabrielli, M. Lipson, and S. G. Johnson, “Transformation inverse design,” Opt. Express **21**, 14223–14243 (2013).
15. A. Y. Piggott, J. Lu, K. G. Lagoudakis, J. Petykiewicz, T. M. Babinec, and J. Vučković, “Inverse design and demonstration of a compact and broadband on-chip wavelength demultiplexer,” Nat. Photonics **9**, 374–377 (2015).
16. R. Bruck, B. Mills, B. Troia, D. J. Thomson, F. Y. Gardes, Y. Hu, G. Z. Mashanovich, V. M. N. Passaro, G. T. Reed, and O. L. Muskens, “Device-level characterization of the flow of light in integrated photonic circuits using ultrafast photomodulation spectroscopy,” Nat. Photonics **9**, 54–60 (2015).
17. A. P. Mosk, A. Lagendijk, G. Lerosey, and M. Fink, “Controlling waves in space and time for imaging and focusing in complex media,” Nat. Photonics **6**, 283–292 (2012).
18. M. Kim, Y. Choi, C. Yoon, W. Choi, J. Kim, Q.-H. Park, and W. Choi, “Maximal energy transport through disordered media with the implementation of transmission eigenchannels,” Nat. Photonics **6**, 581–585 (2012).
19. T. Strudley, R. Bruck, B. Mills, and O. L. Muskens, “An ultrafast reconfigurable nanophotonic switch using wavefront shaping of light in a nonlinear nanomaterial,” Light Sci. Appl. **3**, e207 (2014).
20. E. Silberstein, P. Lalanne, J. P. Hugonin, and Q. Cao, “Use of grating theory in integrated optics,” J. Opt. Soc. Am. A. **18**, 2865–2875 (2001).
21. J. Leuthold and C. H. Joyner, “Multimode interference couplers with tunable power splitting ratios,” J. Lightwave Technol. **19**, 700–707 (2001).
22. S. Nagai, G. Morishima, H. Inayoshi, and K. Utaka, “Multimode interference photonic switches (MIPS),” J. Lightwave Technol. **20**, 675–681 (2002).
23. A. M. Al-hetar, A. S. M. Supaat, A. B. Mohammad, and I. Yulianti, “Multimode interference photonic switches,” Opt. Eng. **47**, 112001 (2008).
24. D. A. May-Arrioja, P. LiKamWa, J. J. Sanchez-Mondragon, R. J. Selvas-Aguilar, and I. Torres-Gomez, “A reconfigurable multimode interference splitter for sensing applications,” Meas. Sci. Technol. **18**, 3241–3246 (2007).
25. A. M. Al-hetar, A. B. Mohammad, A. S. M. Supaat, Z. A. Shamsan, and I. Yulianti, “Fabrication and characterization of polymer thermo-optic switch based on MMI coupler,” Opt. Commun. **284**, 1181–1185 (2011).
26. D. J. Thomson, Y. Hu, G. T. Reed, and J. M. Fedeli, “Low loss MMI couplers for high performance MZI modulators,” IEEE Photon. Technol. Lett. **22**, 1485–1487 (2010).
27. N. M. Wright, D. J. Thomson, K. L. Litvinenko, W. R. Headley, A. J. Smith, A. P. Knights, J. H. B. Deane, F. Y. Gardes, G. Z. Mashanovich, R. Gwilliam, and G. T. Reed, “Free carrier lifetime modification for silicon waveguide based devices,” Opt. Express **16**, 19779–19784 (2008).
28. T. J. Johnson and O. J. Painter, “Passive modification of free carrier lifetime in high-Q silicon-on-insulator optics,” in *Conference on Lasers and Electro-Optics/International Quantum Electronics Conference*, OSA Technical Digest (CD) (Optical Society of America, 2009), paper CFF4.
29. H. Rong, R. Jones, A. Liu, O. Cohen, D. Hak, A. Fang, and M. Paniccia, “A continuous-wave Raman silicon laser,” Nature **433**, 725–728 (2005).
30. D. Brady and D. Psaltis, “Control of volume holograms,” J. Opt. Soc. Am. A **9**, 1167–1182 (1992).
31. J. Capmany, I. Gasulla, and D. Pérez, “Microwave photonics: the programmable processor,” Nat. Photonics **10**, 6–8 (2016).
32. L. Zhuang, C. G. H. Roeloffzen, M. Hoekman, K.-J. Boller, and A. J. Lowery, “Programmable photonic signal processor chip for radiofrequency applications,” Optica **2**, 854–859 (2015).
33. http://dx.doi.org/10.5258/SOTON/384788.